COMPDYN 2013
4th ECCOMAS Thematic Conference on
Computational Methods in Structural Dynamics and Earthquake Engineering
M. Papadrakakis, V. Papadopoulos, V. Plevris (eds.)
Kos Island, Greece, 12–14 June 2013

COUPLING OF FINITE ELEMENTS AND HIERARCHICAL BOUNDARY ELEMENTS FOR DYNAMIC SOIL–STRUCTURE INTERACTION PROBLEMS

Pieter Coulier, Stijn François, Geert Lombaert, and Geert Degrande

KU Leuven, Department of Civil Engineering
Kasteelpark Arenberg 40, 3001 Leuven, Belgium
e-mail: {pieter.coulier,stijn.francois,geert.lombaert,geert.degrande}@bwk.kuleuven.be

Keywords: FE–BE coupling, iterative methods, interface relaxation, $\mathscr{H}$–matrices, dynamic soil–structure interaction.

Abstract. *This paper discusses the coupling of finite element and fast boundary element methods based on hierarchical matrices to solve problems of visco–elastodynamic wave propagation involving dynamic soil–structure interaction in the frequency domain. Three coupling methodologies are presented and their computational performance is assessed through numerical examples. It is demonstrated that a direct coupling approach, in which the boundary element domain is condensed into an equivalent dynamic stiffness matrix, is the least efficient. Iterative procedures provide a valuable alternative; the efficiency of these algorithms strongly depends on the kind of boundary conditions applied to each subdomain, however. The fastest convergence is observed if Neumann boundary conditions are imposed on the most stiff subdomain. Aitken's Δ^2–method is employed in these schemes for the calculation of an optimized interface relaxation parameter in order to ensure and speed up the convergence. A monolithic coupling approach is presented as well, providing a simultaneous solution of the governing equations while avoiding the assembly of a dynamic soil stiffness matrix.*

1 INTRODUCTION

The numerical prediction of three–dimensional (3D) visco–elastodynamic wave propagation in a stratified halfspace arises in a variety of problems, such as the simulation of seismic site effects [1], the modelling of railway induced vibrations [2] and other applications involving dynamic soil–structure interaction (SSI) [3]. A domain decomposition approach is often introduced in computational models, where distinct numerical methods are used for different subdomains. A well–known methodology is the coupled finite element – boundary element (FE–BE) approach, which combines the flexibility offered by the FE method to model complex geometries with the possibility to take the radiation of waves towards infinity into account by means of the BE method. The complementarity of both methods can either be exploited in the time [4] or in the frequency domain [5].

In the past decades, the development of efficient algorithms for the coupling of FE and BE methods has been the subject of numerous investigations [6, 7, 8]. Direct and iterative coupling methodologies exist; the former requires the assembly of a global set of coupled equations, while the governing equations are solved separately in the latter approach. Conforming or non–conforming interface discretizations can be distinguished, imposing the coupling conditions in a strong or weak sense, respectively. The latter allows for an independent mesh size adaptation for each subdomain. FE–BE coupling algorithms for elastostatics are discussed, among others, by Elleithy et al. [9] and Margonari et al. [10], while Rüberg et al. [11] present an algorithm for time–domain elastodynamics using non-conforming interfaces where the coupling conditions are incorporated in a weak sense by means of Lagrange multipliers.

The applicability of classical BE formulations to large scale problems is hindered, however, due to stringent memory and CPU requirement resulting from the dense, fully populated unsymmetric matrices arising in the formulation. This has led to the development of fast BE methods to improve the computational efficiency, including the fast multipole method (FMM) [12] and methods based on hierarchical matrices ($\mathscr{H}$–matrices) [13]. Recently, a $\mathscr{H}$-BE method for visco–elastodynamics in the frequency domain incorporatings Green's functions for a horizontally layered halfspace has been presented [14]. These Green's functions are computed by means of the direct stiffness method [15], as no closed form analytical expressions are available; their application avoids meshing of the free surface and the layer interfaces in the modelling of wave propagation in a stratified medium.

This paper focuses on the coupling of FE and $\mathscr{H}$-BE methods for the solution of dynamic SSI problems. Various FE–$\mathscr{H}$-BE coupling procedures are presented and their computational performance is assessed. Throughout this paper, non–overlapping domains with conforming interface meshes are considered, and all methods are formulated in the frequency domain. The text is organized as follows. Section 2 briefly summarizes the governing equations of the FE and $\mathscr{H}$-BE method. Three different FE–$\mathscr{H}$-BE coupling procedures are subsequently introduced in section 3. First, a classical direct coupling strategy is discussed, which requires the assembly of a dynamic soil stiffness matrix. Next, iterative algorithms are presented; special attention is paid to optimized interface relaxation techniques in order to ensure and/or speed up the convergence. Finally, a monolithic coupling approach is proposed. Numerical examples are investigated in section 4 to validate the coupling strategies and to provide additional insight in the effectiveness of the algorithms. This allows for the formulation of guidelines concerning the choice of an appropriate coupling strategy for a specific dynamic SSI problem.

2 FINITE ELEMENT AND BOUNDARY ELEMENT METHODS

The governing equations of the FE and $\mathscr{H}$-BE method are summarized in this section. It is assumed in the following that finite elements are used to model a structural domain Ω, while boundary elements are employed to model wave propagation in the surrounding soil domain Ω_{s}. The domain Ω should be understood as a generalized structure, which could comprise the actual structure and part of the soil domain. The soil–structure interface is denoted as Σ.

2.1 Finite element formulation

Finite element equilibrium equations of a domain Ω can be obtained by introducing a FE discretization in the weak variational formulation of the equilibrium of Ω, and subsequently applying a Galerkin procedure. This provides the following set of equations [3]:

$$\left[\mathbf{K} + i\omega\widehat{\mathbf{C}}(\omega) - \omega^2\mathbf{M}\right]\hat{\underline{\mathbf{u}}}(\omega) = \hat{\underline{\mathbf{f}}}(\omega) \tag{1}$$

where a hat above a variable denotes its representation in the frequency domain. $\hat{\underline{\mathbf{u}}}(\omega)$ collects the nodal degrees of freedom, while $\mathbf{K}$ and $\mathbf{M}$ are the frequency independent stiffness and mass matrices; the damping matrix $\widehat{\mathbf{C}}(\omega)$ might be frequency dependent. The bracketed term on the left hand side of equation (1) is identified as the dynamic stiffness matrix $\widehat{\mathbf{K}}(\omega)$ of the structure. The vector $\hat{\underline{\mathbf{f}}}(\omega)$ represents the force excitation to which the structure is subjected. Adequate solvers which account for the sparsity and symmetry of the system can be employed to solve equation (1).

2.2 Hierarchical boundary element formulation

The BE method is based on the discretization of the boundary Σ of a domain Ω_{s} with an appropriate number of boundary elements in order to numerically solve a (regularized) boundary integral equation. The method leads to a reduction of the spatial problem dimension (i.e. surface instead of volume discretization), but the storage of the resulting BE collocation matrices requires a quadratic amount of memory with respect to the number of degrees of freedom N_{DOF}, while a cubic amount of numerical operations is needed to solve the corresponding set of BE equations by means of direct numerical solvers. The use of $\mathscr{H}$–matrices provides an elegant way to treat fully populated matrices with almost linear complexity [16], as they approximate the original matrices (with an arbitrary prescribed accuracy) by means of data–sparse, memory–efficient representations. The construction of $\mathscr{H}$–matrices is based on the identification of admissible and inadmissible hierarchical cluster pairs in the BE mesh; the partially pivoted adaptive cross approximation (ACA) algorithm [17, 18] is employed to compute low rank approximations of matrix blocks corresponding to admissible cluster pairs. A major advantage of ACA is its purely algebraic character, avoiding the need for (semi–)analytical expressions of the Green's functions employed in the BE formulation (e.g. allowing for the incorporation of Green's functions for a horizontally layered halfspace [14]). The reader is referred to the literature [13, 16, 19] for a detailed description of the methodology regarding $\mathscr{H}$–matrices. All BE methods discussed in the remainder of this paper involve to application of $\mathscr{H}$–matrices.

For an unbounded domain Ω_{s}, the displacements $\hat{\underline{\mathbf{u}}}(\omega)$ and tractions $\hat{\underline{\mathbf{t}}}(\omega)$ at the collocation points of the boundary Σ are related as follows in the $\mathscr{H}$-BE method:

$$\left[\widehat{\mathbf{T}}_{\mathscr{H}}(\omega) + \mathbf{I}\right]\hat{\underline{\mathbf{u}}}(\omega) = \widehat{\mathbf{U}}_{\mathscr{H}}(\omega)\hat{\underline{\mathbf{t}}}(\omega) \tag{2}$$

where $\widehat{\mathbf{T}}_{\mathscr{H}}(\omega)$ and $\widehat{\mathbf{U}}_{\mathscr{H}}(\omega)$ are hierarchical representations of the BE collocation matrices $\widehat{\mathbf{T}}(\omega)$ and $\widehat{\mathbf{U}}(\omega)$, respectively, while $\mathbf{I}$ represents a unit matrix. The computation of $\widehat{\mathbf{T}}_{\mathscr{H}}(\omega)$ and $\widehat{\mathbf{U}}_{\mathscr{H}}(\omega)$ requires integration of the Green's tractions and displacements over the boundary Σ. Equation (2) can be rewritten as:

$$\widehat{\mathbf{A}}_{\mathscr{H}}(\omega)\hat{\underline{\mathbf{x}}}(\omega) = \hat{\underline{\mathbf{b}}}(\omega) \tag{3}$$

where the vector of unknowns $\hat{\underline{\mathbf{x}}}(\omega)$ contains displacements, tractions or both, depending on whether a Neumann, Dirichlet or mixed Neumann–Dirichlet problem is considered, respectively. In order to solve equation (3), iterative Krylov subspace methods such as the generalized minimal residual method (GMRES) [20] are well suited. The matrix–vector multiplication forms the core of iterative solvers, and the complexity of this operation is only $\mathcal{O}(N_{\text{DOF}} \log N_{\text{DOF}})$ for $\mathscr{H}$–matrices [19]. A tolerance of 10^{-6} is specified in the iterative solver for the relative residual norm $||\hat{\underline{\mathbf{b}}}(\omega) - \widehat{\mathbf{A}}_{\mathscr{H}}(\omega)\hat{\underline{\mathbf{x}}}(\omega)||_2/||\hat{\underline{\mathbf{b}}}(\omega)||_2$ in all numerical examples presented in this paper.

As will be clarified in section 3, equation (3) has to be solved multiple times with a varying right hand side $\hat{\underline{\mathbf{b}}}(\omega)$ in FE–$\mathscr{H}$-BE coupling algorithms, and the implementation of a suitable preconditioner is therefore desirable to reduce the computation time. A right preconditioner $\widehat{\mathbf{M}}(\omega)$ is used throughout this paper in order to lower the condition number of the coefficient matrix $\widehat{\mathbf{A}}_{\mathscr{H}}(\omega)$:

$$\widehat{\mathbf{A}}_{\mathscr{H}}(\omega)\widehat{\mathbf{M}}^{-1}(\omega)\hat{\underline{\mathbf{y}}}(\omega) = \hat{\underline{\mathbf{b}}}(\omega) \tag{4}$$

with $\widehat{\mathbf{M}}(\omega)\hat{\underline{\mathbf{x}}}(\omega) = \hat{\underline{\mathbf{y}}}(\omega)$. An example of an efficient preconditioner is the approximate $\mathscr{H}$–LU decomposition proposed in [21]; its computation requires, however, additional arithmetic operations. A much simpler strategy is applied in this paper, following the approach recently adopted by Chaillat et al. for the acceleration of FMM calculations for elastodynamics [23]. A block diagonal preconditioner $\widehat{\mathbf{M}}(\omega) = \text{blkdiag}\left(\widehat{\mathbf{A}}_{\mathscr{H}}(\omega)\right)$ is employed, where the size of the diagonal blocks is determined by the lowest hierarchical cluster level. An inner GMRES solver with a moderate tolerance of 10^{-2} is applied to solve the preconditioning linear systems, resulting in a nested inner–outer iteration scheme. Furthermore, the flexible GMRES (FGMRES) algorithm [22] is employed for the outer iteration in order to avoid the explicit application of $\widehat{\mathbf{M}}^{-1}(\omega)$ to the Krylov vectors. As $\widehat{\mathbf{M}}(\omega)$ is already computed and stored, the proposed approach is very cheap in terms of computational resources.

3 FE–$\mathscr{H}$-BE COUPLING PROCEDURES

Three procedures for the coupling of FE and $\mathscr{H}$-BE models are outlined in this section. The numerical validation and the assessment of the computational efficiency of the proposed methods are subsequently addressed in section 4.

3.1 Direct FE–$\mathscr{H}$-BE coupling

In a classical direct coupling strategy [24], the governing equations of the FE and BE subdomain are straightforwardly combined, accounting for continuity of displacements and equilibrium of tractions at the soil–structure interface Σ. This results in a global coupled system of equations:

$$\left(\begin{bmatrix}\widehat{\mathbf{K}}_{11}(\omega) & \widehat{\mathbf{K}}_{12}(\omega)\\ \widehat{\mathbf{K}}_{21}(\omega) & \widehat{\mathbf{K}}_{22}(\omega)\end{bmatrix} + \begin{bmatrix}\mathbf{0} & \mathbf{0}\\ \mathbf{0} & \widehat{\mathbf{K}}^{\text{s}}_{22}(\omega)\end{bmatrix}\right)\begin{Bmatrix}\hat{\underline{\mathbf{u}}}_1(\omega)\\ \hat{\underline{\mathbf{u}}}_2(\omega)\end{Bmatrix} = \begin{Bmatrix}\hat{\underline{\mathbf{f}}}_1(\omega)\\ \hat{\underline{\mathbf{f}}}_2(\omega)\end{Bmatrix} \tag{5}$$

where a subdivision into block matrices according to degrees of freedom $\underline{\hat{\mathbf{u}}}_2(\omega)$ on the soil–structure interface Σ and degrees of freedom $\underline{\hat{\mathbf{u}}}_1(\omega)$ internally in the structural domain Ω is introduced. $\widehat{\mathbf{K}}^{\mathrm{s}}_{22}(\omega)$ represents the dynamic soil stiffness matrix and is defined as:

$$\widehat{\mathbf{K}}^{\mathrm{s}}_{22}(\omega) = \int_{\Sigma} \mathbf{N}_2^{\mathrm{T}}(\mathbf{x})\mathbf{N}_2(\mathbf{x})\underline{\hat{\mathbf{t}}}(\mathbf{N}_2(\mathbf{x}))(\omega)\,\mathrm{d}S = \mathbf{T}_{\mathrm{q}}\,\underline{\hat{\mathbf{t}}}(\mathbf{N}_2(\mathbf{x}))(\omega) \tag{6}$$

where $\mathbf{N}_2(\mathbf{x})$ indicates the FE shape functions on the soil–structure interface Σ, corresponding to the BE interpolation functions (as conforming FE and BE meshes are considered). The frequency independent matrix $\mathbf{T}_{\mathrm{q}} = \int_{\Sigma} \mathbf{N}_2^{\mathrm{T}}(\mathbf{x})\mathbf{N}_2(\mathbf{x})\,\mathrm{d}S$ links the FE and BE discretizations.

Although equation (5) provides a straightforward solution to the dynamic SSI problem, it suffers from some major drawbacks. Equation (6) requires the evaluation of tractions $\underline{\hat{\mathbf{t}}}(\mathbf{N}_2(\mathbf{x}))(\omega)$ by means of the $\mathscr{H}$-BE method, which implies that equation (4) has to be solved for multiple right hand sides (i.e. for all shape functions $\mathbf{N}_2(\mathbf{x})$ on Σ); the implemented FGMRES algorithm is only able to handle one right hand side at a time. Furthermore, addition of the dense unsymmetric dynamic soil stiffness matrix $\widehat{\mathbf{K}}^{\mathrm{s}}_{22}(\omega)$ to $\widehat{\mathbf{K}}(\omega)$ strongly affects the sparsity of the system, reducing the efficiency of sparse finite element solvers applied to equation (5). The numerical examples in section 4 will demonstrate that this conventional approach, in which the dynamic soil stiffness matrix $\widehat{\mathbf{K}}^{\mathrm{s}}_{22}(\omega)$ is explicitly evaluated, does not provide an efficient solution procedure, especially in case large scale problems are considered.

3.2 Iterative FE–$\mathscr{H}$-BE coupling

Iterative coupling procedures provide a valuable alternative to the conventional direct strategy outlined in the previous subsection, as the evaluation of the dynamic soil stiffness matrix $\widehat{\mathbf{K}}^{\mathrm{s}}_{22}(\omega)$ is avoided. The governing equations are solved separately for each subdomain in such an approach, while the boundary conditions at the soil–structure interface are updated until convergence is achieved. This methodology avoids the assembly and solution of a global system of coupled equations; it hence allows for the coupling of black box FE and $\mathscr{H}$-BE solvers. Iterative schemes are often used for dynamic SSI problems in the time domain to allow for the use of different time discretization schemes [4, 25, 26]. Their application in the frequency domain remains rather limited, however, especially due to convergence difficulties [27]. Frequency domain iterative algorithms described in the literature mainly involve acoustic–acoustic [28] and acoustic–elastodynamic [27] coupling, although Grasso [29] discusses the iterative coupling of FE and fast multipole BE models for visco–elastodynamics in the frequency domain.

Four different iterative algorithms for the coupling of FE and $\mathscr{H}$-BE model are outlined in the following subsections. These methodologies are denoted as sequential Neumann–Dirichlet or Dirichlet–Neumann algorithms, and parallel Neumann–Neumann or Dirichlet–Dirichlet algorithms, respectively, indicating which kind of boundary conditions are imposed on the FE and BE subdomain.

3.2.1 Sequential Neumann–Dirichlet algorithm

At iteration step k of the sequential Neumann–Dirichlet procedure, the finite element subdomain is analyzed with Neumann boundary conditions $\underline{\hat{\mathbf{q}}}^{(k)}(\omega)$ at the soil–structure interface Σ:

$$\begin{bmatrix} \widehat{\mathbf{K}}_{11}(\omega) & \widehat{\mathbf{K}}_{12}(\omega) \\ \widehat{\mathbf{K}}_{21}(\omega) & \widehat{\mathbf{K}}_{22}(\omega) \end{bmatrix} \begin{Bmatrix} \underline{\hat{\mathbf{u}}}_1^{(k)}(\omega) \\ \underline{\hat{\mathbf{u}}}_2^{(k)}(\omega) \end{Bmatrix} = \begin{Bmatrix} \underline{\hat{\mathbf{f}}}_1(\omega) \\ \underline{\hat{\mathbf{f}}}_2(\omega) \end{Bmatrix} + \begin{Bmatrix} \underline{\mathbf{0}} \\ \underline{\hat{\mathbf{q}}}^{(k)}(\omega) \end{Bmatrix} \tag{7}$$

where $\underline{\hat{\mathbf{q}}}^{(k)}(\omega)$ denotes the soil–structure interaction forces. Solving equation (7) by means of a standard finite element solver provides the internal and interface displacements $\underline{\hat{\mathbf{u}}}_1^{(k)}(\omega)$ and $\underline{\hat{\mathbf{u}}}_2^{(k)}(\omega)$. The latter are subsequently imposed as Dirichlet boundary conditions on the boundary element subdomain, allowing to solve the preconditioned system of equations (4) for the interface tractions $\underline{\hat{\mathbf{t}}}^{(k)}(\omega)$ using the FGMRES solver. These tractions are used to calculate equivalent nodal forces $\underline{\hat{\mathbf{q}}}^{(k+\lambda)}(\omega)$:

$$\underline{\hat{\mathbf{q}}}^{(k+\lambda)}(\omega) = -\int_{\Sigma} \mathbf{N}_2^{\mathrm{T}}(\mathbf{x})\mathbf{N}_2(\mathbf{x})\underline{\hat{\mathbf{t}}}^{(k)}(\omega)\,\mathrm{d}S = -\mathbf{T}_{\mathrm{q}}\,\underline{\hat{\mathbf{t}}}^{(k)}(\omega) \tag{8}$$

The interaction forces are finally relaxed using an iteration dependent relaxation parameter $\lambda^{(k)}$:

$$\underline{\hat{\mathbf{q}}}^{(k+1)}(\omega) = \lambda^{(k)}\underline{\hat{\mathbf{q}}}^{(k+\lambda)}(\omega) + (1-\lambda^{(k)})\underline{\hat{\mathbf{q}}}^{(k)}(\omega) \tag{9}$$

Once the relaxed interaction forces $\underline{\hat{\mathbf{q}}}^{(k+1)}(\omega)$ are computed, a subsequent step in the iterative procedure is performed until convergence is obtained; an accuracy of 10^{-4} is prescribed for the relative residual norm $||\underline{\hat{\mathbf{u}}}_2^{(k+1)}(\omega) - \underline{\hat{\mathbf{u}}}_2^{(k)}(\omega)||_2 / ||\underline{\hat{\mathbf{u}}}_2^{(k+1)}(\omega)||_2$ of the interface displacements and $||\underline{\hat{\mathbf{q}}}^{(k+1)}(\omega) - \underline{\hat{\mathbf{q}}}^{(k)}(\omega)||_2 / ||\underline{\hat{\mathbf{q}}}^{(k+1)}(\omega)||_2$ of the interaction forces.

The choice of a suitable relaxation parameter $\lambda^{(k)}$ in equation (9) is of great importance in order to ensure and/or speed up the convergence of the iterative algorithm. Constant relaxation parameters are considered, among others, by Elleithy et al. [9, 30] for linear elastostatics, von Estorff et al. [4] for transient elastodynamics, Hagen [31] for fluid–soil–structure interaction, and Grasso [29] for visco–elastodynamics in the frequency domain. Convergence conditions have been established [9, 30] and parametric studies have been performed to identify the optimal choice of a constant relaxation parameter [4, 31]. Soares et al. [27] present an iterative procedure for the solution of fluid–solid interaction problems in the frequency domain, in which an optimized relaxation parameter is calculated in each iterative step by minimizing the square error functional of the interface fluxes.

In this paper, Aitken's Δ^2–method [32] is employed for the determination of an iteration dependent relaxation parameter $\lambda^{(k)}$. This method provides a simple but efficient procedure to determine $\lambda^{(k)}$, based on the results of two subsequent iterations. It is often applied in the iterative solution of fluid–structure interaction problems [33, 34] and has already been adopted for transient elastodynamic problems [26]. Figure 1a shows a graphical illustration of the main idea behind this method, for a general iteration process in terms of a scalar x and a function $f(x)$, with solution $\overline{x} = f(\overline{x})$. An estimation $x^{(k+\lambda)} = f(x^{(k)})$ is computed in step k of the iterative procedure; if no relaxation is applied (i.e. $\lambda^{(k)} \equiv 1$), the new approximation of $\overline{x}$ yields $x^{(k+1)} = x^{(k+\lambda)}$. In Aitken's Δ^2–method, however, the estimation $x^{(k+\lambda)} = f(x^{(k)})$ is combined with the result of the previous iteration step $k-1$, which allows for the determination of $x^{(k+1)}$ as the intersection of the linearized function $\tilde{f}^{(k)}(x)$ through the points $\left\{x^{(k-1)}, x^{(k-1+\lambda)}\right\}^{\mathrm{T}}$ and $\left\{x^{(k)}, x^{(k+\lambda)}\right\}^{\mathrm{T}}$, and the function $y = x$, respectively. This clearly corresponds to a single step of the secant method [34]. The relaxation parameter $\lambda^{(k)}$ can hence be written in function of $x^{(k-1)}$, $x^{(k-1+\lambda)}$, $x^{(k)}$ and $x^{(k+\lambda)}$:

$$\lambda^{(k)} = \frac{x^{(k)} - x^{(k-1)}}{x^{(k)} - x^{(k+\lambda)} - x^{(k-1)} + x^{(k-1+\lambda)}} \tag{10}$$

Introducing the relation $x^{(k)} - x^{(k-1)} = \lambda^{(k-1)}\left(x^{(k-1+\lambda)} - x^{(k-1)}\right)$ provides a recursive relation

for the relaxation parameter $\lambda^{(k)}$:

$$\lambda^{(k)} = \lambda^{(k-1)} \frac{x^{(k-1+\lambda)} - x^{(k-1)}}{x^{(k)} - x^{(k+\lambda)} - x^{(k-1)} + x^{(k-1+\lambda)}} \tag{11}$$

$$= -\lambda^{(k-1)} \frac{r^{(k-1)}}{r^{(k)} - r^{(k-1)}} \tag{12}$$

with the residual $r^{(k)}$ defined as $r^{(k)} = x^{(k)} - x^{(k+\lambda)}$.

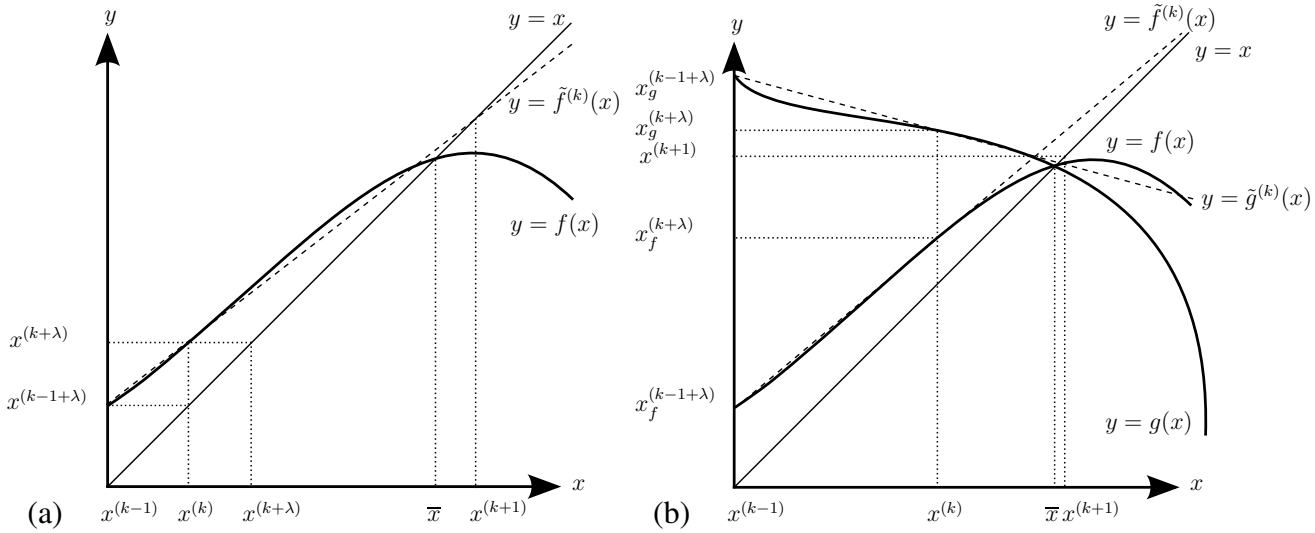

Figure 1: Graphical illustration of Aitken's Δ^2–method employed in (a) sequential and (b) parallel iterative algorithms.

For the vectorized interaction forces $\hat{\underline{\mathbf{q}}}(\omega)$ considered in this subsection, however, the division in equation (12) is impossible. Following the approach presented by Irons and Tuck [35], the vectors are projected in the direction $\hat{\underline{\mathbf{r}}}^{(k)}(\omega) - \hat{\underline{\mathbf{r}}}^{(k-1)}(\omega) = \hat{\underline{\mathbf{q}}}^{(k)}(\omega) - \hat{\underline{\mathbf{q}}}^{(k+\lambda)}(\omega) - \hat{\underline{\mathbf{q}}}^{(k-1)}(\omega) + \hat{\underline{\mathbf{q}}}^{(k-1+\lambda)}(\omega)$:

$$\lambda^{(k)} = -\lambda^{(k-1)} \frac{\left(\hat{\underline{\mathbf{r}}}^{(k)}(\omega) - \hat{\underline{\mathbf{r}}}^{(k-1)}(\omega)\right)^{\mathrm{T}} \hat{\underline{\mathbf{r}}}^{(k-1)}(\omega)}{||\hat{\underline{\mathbf{r}}}^{(k)}(\omega) - \hat{\underline{\mathbf{r}}}^{(k-1)}(\omega)||^2} \tag{13}$$

with $\lambda^{(0)} = 1$. Equation (13) can be evaluated at low computational cost, providing a simple and robust way to calculate an iteration dependent relaxation parameter, hence avoiding the need for an empirical trial–and–error process [4]. As all calculations are performed in the frequency domain, the relaxation parameter $\lambda^{(k)}$ is a complex number. Although the amplitude of this number could be limited (e.g. $||\lambda^{(k)}|| \leq 1$), it is chosen not to do so in this paper, as Soares et al. [27] have observed that faster convergence could be achieved with a non–restricted relaxation parameter (in case of acoustic–elastodynamic FE–BE coupling in the frequency domain).

The convergence of the algorithm can be further accelerated by using the relaxed tractions $-\mathbf{T}_{\mathrm{q}}^{-1}\, \hat{\underline{\mathbf{q}}}^{(k)}(\omega)$ obtained in iteration $k-1$ as an initial guess in the iterative FGMRES algorithm employed to solve equation (4) for $\hat{\underline{\mathbf{t}}}^{(k)}(\omega)$ in iteration k. Furthermore, if a loop with a sufficiently fine frequency sampling is considered, the converged solution at a particular frequency can be used as an initial guess for the first iteration at the subsequent frequency.

A major disadvantage of the proposed algorithm lies in the fact that it does not allow to determine the static solution, as application of Neumann boundary conditions to the unconstrained structural domain Ω results in a singularity of the FE equations. The convergence behaviour at low frequencies is hence expected to be poor, and the frequency sweep is therefore performed from high to low frequencies. Singularity of the FE equations is also encountered if the structure is excited at one of its (undamped) natural frequencies; incorporation of structural damping remediates this issue.

3.2.2 Sequential Dirichlet–Neumann algorithm

The second iterative algorithm considered in this paper consist of a sequential Dirichlet–Neumann scheme; the type of boundary conditions applied to each subdomain is reversed compared to the procedure outlined in subsection 3.2.1. At iteration step k, Dirichlet boundary conditions $\underline{\hat{\mathbf{u}}}_2^{(k)}(\omega)$ are imposed on the interface Σ of the FE subdomain, providing the interaction forces $\underline{\hat{\mathbf{q}}}^{(k)}(\omega)$ through the solution of equation (7) (and condensation of the internal degrees of freedom $\underline{\hat{\mathbf{u}}}_1^{(k)}(\omega)$). The corresponding interface tractions $\underline{\hat{\mathbf{t}}}^{(k)}(\omega) = -\mathbf{T}_{\mathrm{q}}^{-1}\,\underline{\hat{\mathbf{q}}}^{(k)}(\omega)$ are applied to the BE subdomain, and unrelaxed interface displacements $\underline{\hat{\mathbf{u}}}_2^{(k+\lambda)}(\omega)$ are obtained by solving the preconditioned system of equations (4) using the FGMRES solver. Aitken's Δ^2–method is finally employed for the determination of an optimized relaxation parameter $\lambda^{(k)}$ (with equation (13) in that case based on interface displacements instead of interaction forces), allowing for the computation of relaxed interface displacements $\underline{\hat{\mathbf{u}}}_2^{(k+1)}(\omega)$. This iterative procedure is repeated until convergence is achieved.

As displacements are imposed on the boundary of the FE subdomain, the iterative scheme also succeeds in solving the coupled problem for static excitation or excitation near a natural frequency (in case of an undamped structure), in contrast to the Neumann–Dirichlet algorithm presented in subsection 3.2.1.

3.2.3 Parallel Neumann–Neumann algorithm

A parallel Neumann–Neumann iterative scheme is obtained if the interaction forces $\underline{\hat{\mathbf{q}}}^{(k)}(\omega)$ and corresponding interface tractions $\underline{\hat{\mathbf{t}}}^{(k)}(\omega) = -\mathbf{T}_{\mathrm{q}}^{-1}\,\underline{\hat{\mathbf{q}}}^{(k)}(\omega)$ are simultaneously imposed as Neumann boundary conditions on the interface Σ of the FE and BE subdomain, respectively. Solving equations (7) and (4) provides (incompatible) interface displacements $\underline{\hat{\mathbf{u}}}_{2,\mathrm{FE}}^{(k)}(\omega)$ and $\underline{\hat{\mathbf{u}}}_{2,\mathrm{BE}}^{(k)}(\omega)$, respectively. The discrepancy of interface displacements $\Delta\underline{\hat{\mathbf{u}}}_2^{(k)}(\omega) = \underline{\hat{\mathbf{u}}}_{2,\mathrm{BE}}^{(k)}(\omega) - \underline{\hat{\mathbf{u}}}_{2,\mathrm{FE}}^{(k)}(\omega)$ is subsequently employed to calculate an increment of interaction forces $\Delta\underline{\hat{\mathbf{q}}}^{(k)}(\omega)$. The displacement discrepancy $\Delta\underline{\hat{\mathbf{u}}}_2^{(k)}(\omega)$ can either be imposed on the FE or the BE subdomain to compute this increment; this either yields unrelaxed interaction forces $\underline{\hat{\mathbf{q}}}_{\mathrm{FE}}^{(k+\lambda)}(\omega) = \underline{\hat{\mathbf{q}}}^{(k)}(\omega) + \Delta\underline{\hat{\mathbf{q}}}_{\mathrm{FE}}^{(k)}(\omega)$ or $\underline{\hat{\mathbf{q}}}_{\mathrm{BE}}^{(k+\lambda)}(\omega) = \underline{\hat{\mathbf{q}}}^{(k)}(\omega) + \Delta\underline{\hat{\mathbf{q}}}_{\mathrm{BE}}^{(k)}(\omega)$. Application of Aitken relaxation finally provides relaxed interaction forces $\underline{\hat{\mathbf{q}}}_{\mathrm{FE}}^{(k+1)}(\omega)$ or $\underline{\hat{\mathbf{q}}}_{\mathrm{BE}}^{(k+1)}(\omega)$, which are used in a subsequent step of the iterative scheme.

One can expect that the fastest convergence will be achieved if the force increment $\Delta\underline{\hat{\mathbf{q}}}^{(k)}(\omega)$ is calculated by imposing the displacement discrepancy $\Delta\underline{\hat{\mathbf{u}}}_2^{(k)}(\omega)$ on the most flexible subdomain. It is difficult, however, to estimate the flexibility of each subdomain a priori, especially as the latter is frequency dependent. Choosing either the FE or the BE subdomain for the calculation of $\Delta\underline{\hat{\mathbf{q}}}^{(k)}(\omega)$ hence requires a profound understanding of the dynamic behaviour of

each subdomain; a wrong choice can significantly deteriorate the convergence of the iterative procedure.

A more robust variant of the algorithm is therefore presented in this paper, where $\underline{\hat{\mathbf{q}}}_{\mathrm{FE}}^{(k+\lambda)}(\omega)$ and $\underline{\hat{\mathbf{q}}}_{\mathrm{BE}}^{(k+\lambda)}(\omega)$ are simultaneously accounted for in the determination of the relaxed interaction forces $\underline{\hat{\mathbf{q}}}^{(k+1)}(\omega)$. The concept is illustrated in figure 1b for a general iteration process in terms of a scalar x and two functions $f(x)$ and $g(x)$, with solution $\overline{x} = f(\overline{x}) = g(\overline{x})$. The basic idea is to apply Aitken relaxation to both $f(x)$ and $g(x)$. At iteration step k, two estimations $x_f^{(k+\lambda)} = f(x^{(k)})$ and $x_g^{(k+\lambda)} = g(x^{(k)})$ are calculated. These estimations are combined with the data points $\{x^{(k-1)}, x_f^{(k-1+\lambda)}\}^{\mathrm{T}}$ and $\{x^{(k-1)}, x_g^{(k-1+\lambda)}\}^{\mathrm{T}}$ obtained in the previous iteration step $k-1$ to define linear approximations $\tilde{f}^{(k)}(x)$ and $\tilde{g}^{(k)}(x)$ of the functions $f(x)$ and $g(x)$, respectively. The ordinate of the intersection of these linearized functions $\tilde{f}^{(k)}(x)$ and $\tilde{g}^{(k)}(x)$ provides a new approximation $x^{(k+1)}$ of the solution $\overline{x}$:

$$x^{(k+1)} = \frac{r_g^{(k)}}{r_g^{(k)} - r_f^{(k)}}\, x_f^{(k+\lambda)} - \frac{r_f^{(k)}}{r_g^{(k)} - r_f^{(k)}}\, x_g^{(k+\lambda)} \tag{14}$$

with $r_f^{(k)} = x_f^{(k+\lambda)} - x_f^{(k-1+\lambda)}$ and $r_g^{(k)} = x_g^{(k+\lambda)} - x_g^{(k-1+\lambda)}$. These residual vectors are defined differently compared to equation (12).

For the vectorized interaction forces $\underline{\hat{\mathbf{q}}}(\omega)$, however, a projection in the direction $\underline{\hat{\mathbf{r}}}_{\mathrm{BE}}^{(k)}(\omega) - \underline{\hat{\mathbf{r}}}_{\mathrm{FE}}^{(k)}(\omega) = \underline{\hat{\mathbf{q}}}_{\mathrm{BE}}^{(k+\lambda)}(\omega) - \underline{\hat{\mathbf{q}}}_{\mathrm{BE}}^{(k-1+\lambda)}(\omega) - \underline{\hat{\mathbf{q}}}_{\mathrm{FE}}^{(k+\lambda)}(\omega) + \underline{\hat{\mathbf{q}}}_{\mathrm{FE}}^{(k-1+\lambda)}(\omega)$ is introduced in equation (14):

$$\begin{aligned}\underline{\hat{\mathbf{q}}}^{(k+1)}(\omega) = {} & \frac{\left(\underline{\hat{\mathbf{r}}}_{\mathrm{BE}}^{(k)}(\omega) - \underline{\hat{\mathbf{r}}}_{\mathrm{FE}}^{(k)}(\omega)\right)^{\mathrm{T}} \underline{\hat{\mathbf{r}}}_{\mathrm{BE}}^{(k)}(\omega)}{||\underline{\hat{\mathbf{r}}}_{\mathrm{BE}}^{(k)}(\omega) - \underline{\hat{\mathbf{r}}}_{\mathrm{FE}}^{(k)}(\omega)||^2}\, \underline{\hat{\mathbf{q}}}_{\mathrm{FE}}^{(k+\lambda)}(\omega) \\ & - \frac{\left(\underline{\hat{\mathbf{r}}}_{\mathrm{BE}}^{(k)}(\omega) - \underline{\hat{\mathbf{r}}}_{\mathrm{FE}}^{(k)}(\omega)\right)^{\mathrm{T}} \underline{\hat{\mathbf{r}}}_{\mathrm{FE}}^{(k)}(\omega)}{||\underline{\hat{\mathbf{r}}}_{\mathrm{BE}}^{(k)}(\omega) - \underline{\hat{\mathbf{r}}}_{\mathrm{FE}}^{(k)}(\omega)||^2}\, \underline{\hat{\mathbf{q}}}_{\mathrm{BE}}^{(k+\lambda)}(\omega)\end{aligned} \tag{15}$$

Equation (15) clearly indicates that $\underline{\hat{\mathbf{q}}}_{\mathrm{FE}}^{(k+\lambda)}(\omega)$ and $\underline{\hat{\mathbf{q}}}_{\mathrm{BE}}^{(k+\lambda)}(\omega)$ are simultaneously accounted for in the determination of a new estimate $\underline{\hat{\mathbf{q}}}^{(k+1)}(\omega)$, with iteration dependent weighting factors based on data of two subsequent iterations; these weighting factors can be calculated at low computational cost. This approach hence avoids the need for a priori information concerning the flexibility of the FE and BE subdomain.

3.2.4 Parallel Dirichlet–Dirichlet algorithm

The final iterative algorithm discussed in this paper is a parallel Dirichlet–Dirichlet strategy, which is very similar to the procedure outlined in subsection 3.2.3. Imposing Dirichlet boundary conditions $\underline{\hat{\mathbf{u}}}_2^{(k)}(\omega)$ on Σ allows for the computation of interaction forces $\underline{\hat{\mathbf{q}}}_{\mathrm{FE}}^{(k)}(\omega)$ and $\underline{\hat{\mathbf{q}}}_{\mathrm{BE}}^{(k)}(\omega)$ through equations (7) and (4), respectively. The resulting force discrepancy $\Delta\underline{\hat{\mathbf{q}}}^{(k)}(\omega) = \underline{\hat{\mathbf{q}}}_{\mathrm{BE}}^{(k)}(\omega) - \underline{\hat{\mathbf{q}}}_{\mathrm{FE}}^{(k)}(\omega)$ is employed to calculate interface displacement increments $\Delta\underline{\hat{\mathbf{u}}}_{2,\mathrm{FE}}^{(k)}(\omega)$ and $\Delta\underline{\hat{\mathbf{u}}}_{2,\mathrm{BE}}^{(k)}(\omega)$, and unrelaxed displacements $\underline{\hat{\mathbf{u}}}_{2,\mathrm{FE}}^{(k+\lambda)}(\omega) = \underline{\hat{\mathbf{u}}}_{2,\mathrm{FE}}^{(k)}(\omega) + \Delta\underline{\hat{\mathbf{u}}}_{2,\mathrm{FE}}^{(k)}(\omega)$ and $\underline{\hat{\mathbf{u}}}_{2,\mathrm{BE}}^{(k+\lambda)}(\omega) = \underline{\hat{\mathbf{u}}}_{2,\mathrm{BE}}^{(k)}(\omega) + \Delta\underline{\hat{\mathbf{u}}}_{2,\mathrm{BE}}^{(k)}(\omega)$ can subsequently be obtained. The relaxed interface displacements $\underline{\hat{\mathbf{u}}}_2^{(k+1)}(\omega)$ are finally computed by means of the relaxation procedure introduced in subsection 3.2.3; equation (15) is in that case based on interface displacements instead of interaction forces. The procedure is repeated until convergence is achieved.

3.3 Monolithic FE–$\mathscr{H}$-BE coupling

A third FE–$\mathscr{H}$-BE coupling approach consists of a monolithic coupling, in which the governing equations of both subdomains are solved simultaneously, while the assembly of a dynamic soil stiffness matrix is avoided. This approach fundamentally differs from the conventional direct coupling approach outlined in subsection 3.1. Combining equations (1) and (2) and accounting for continuity of displacements and equilibrium of tractions at the soil–structure interface Σ yields:

$$\begin{bmatrix} \widehat{\mathbf{K}}_{11}(\omega) & \widehat{\mathbf{K}}_{12}(\omega) & \mathbf{0} \\ \widehat{\mathbf{K}}_{21}(\omega) & \widehat{\mathbf{K}}_{22}(\omega) & \mathbf{T}_{\mathrm{q}} \\ \mathbf{0} & \widehat{\mathbf{T}}_{\mathscr{H}}(\omega) + \mathbf{I} & -\widehat{\mathbf{U}}_{\mathscr{H}}(\omega) \end{bmatrix} \begin{Bmatrix} \underline{\hat{\mathbf{u}}}_1(\omega) \\ \underline{\hat{\mathbf{u}}}_2(\omega) \\ \underline{\hat{\mathbf{t}}}(\omega) \end{Bmatrix} = \begin{Bmatrix} \underline{\hat{\mathbf{f}}}_1(\omega) \\ \underline{\hat{\mathbf{f}}}_2(\omega) \\ \underline{\mathbf{0}} \end{Bmatrix} \tag{16}$$

where the coupling matrix $\mathbf{T}_{\mathrm{q}}$ is defined as in equation (6). The system size in this monolithic approach is significantly larger than in the classical direct coupling strategy of subsection 3.1. The coefficient matrix is never assembled explicitly, however, as equation (16) is solved by means of an iterative GMRES solver. This requires an efficient evaluation of the matrix–vector product, indicating that the monolithic formulation (16) is only advantageous if a fast BE method (i.c. a formulation based on $\mathscr{H}$–matrices) is employed. Although Margonari et al. [10] have used a monolithic approach for the coupling of FE and fast multipole BE models for elastostatics, it is rarely used in elastodynamics [29]. This strategy is often applied for solving strongly coupled fluid–structure interaction problems [36, 37], however, as the discretization methods commonly used for the fluid and the structure lead to sparse matrices.

The coefficient matrix in equation (16) is likely to be ill–conditioned, as the matrix entries arising from the FE and BE discretizations differ by several orders of magnitude. Convergence of the iterative solver will therefore be slow, and the incorporation of a suitable preconditioner is indispensable. Following simple right preconditioner $\widehat{\mathbf{M}}(\omega)$ is employed:

$$\widehat{\mathbf{M}}(\omega) = \begin{bmatrix} \mathrm{diag}\left(\widehat{\mathbf{K}}_{11}(\omega)\right) & \mathbf{0} & \mathbf{0} \\ \mathbf{0} & \mathrm{diag}\left(\widehat{\mathbf{K}}_{22}(\omega)\right) & \mathbf{T}_{\mathrm{q}} \\ \mathbf{0} & \mathrm{blkdiag}\left(\widehat{\mathbf{T}}_{\mathscr{H}}(\omega)\right) + \mathbf{I} & \mathrm{blkdiag}\left(-\widehat{\mathbf{U}}_{\mathscr{H}}(\omega)\right) \end{bmatrix} \tag{17}$$

where the size of the diagonal blocks of $\widehat{\mathbf{T}}_{\mathscr{H}}(\omega)$ and $\widehat{\mathbf{U}}_{\mathscr{H}}(\omega)$ is determined by the lowest hierarchical BE cluster level. The nested FGMRES solution procedure discussed in subsection 2.2 is employed here as well, avoiding the explicit assembly of $\widehat{\mathbf{M}}^{-1}(\omega)$.

4 NUMERICAL EXAMPLES

In the following subsections, two examples are considered to validate the numerical implementation of the proposed FE–$\mathscr{H}$-BE coupling algorithms and to assess their computational performance. While the first example is related to a full space geometry, the second example involves Green's functions for a layered halfspace. All calculations have been performed on Intel® Xeon® E5520 (2.26 GHz) CPUs.

4.1 3D spherical cavity surrounded by a spherical layer and a full space subjected to an internal pressure

Consider a 3D spherical cavity with inner radius $r_{\mathrm{i}} = 1\,\mathrm{m}$ surrounded by a spherical layer with outer radius $r_{\mathrm{o}} = 2\,\mathrm{m}$ and embedded in a homogeneous full space, which is loaded by

an internal pressure $\hat{p}(\omega) = 1\,\mathrm{Pa/Hz}$ (figure 2a). The full space is characterized by a shear wave velocity $C_\mathrm{s} = 150\,\mathrm{m/s}$, a dilatational wave velocity $C_\mathrm{p} = 300\,\mathrm{m/s}$ and a density $\rho = 1800\,\mathrm{kg/m^3}$. Material damping ratios $\beta_\mathrm{s} = \beta_\mathrm{p} = 0.025$ in both deviatoric and volumetric deformation are specified. The wave velocities in the spherical layer are defined as $\alpha C_{\mathrm{s,full}}$ and $\alpha C_{\mathrm{p,full}}$ (with $C_{\mathrm{s,full}}$ and $C_{\mathrm{p,full}}$ the wave velocities in the full space), respectively, where following values are considered for the ratio α: (i) $\alpha = 1/2$, (ii) $\alpha = 1$ and (iii) $\alpha = 2$. The same material damping ratios and density as in the full space are used.

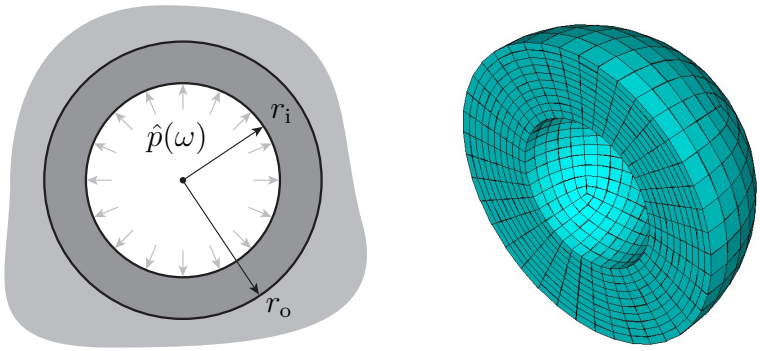

Figure 2: (a) 3D spherical cavity surrounded by a spherical layer with inner radius r_i and outer radius r_o and a homogeneous full space, subjected to an internal pressure $\hat{p}(\omega)$, and (b) half of the FE discretization of the spherical layer.

The spherical layer is discretized by means of 6000 eight–node solid finite elements, which are coupled to a conforming BE mesh consisting of 600 four–node quadrilateral elements for the surrounding full space (figure 2b). A nodal collocation scheme is used for the latter to facilitate the FE–BE coupling, resulting in 19866 FE and 1806 BE degrees of freedom. Up to 6.67 elements per dilatational wavelength $\lambda_\mathrm{p} = C_\mathrm{p}/f$ are provided at a frequency of $100\,\mathrm{Hz}$ in case (i). Analytical full space fundamental solutions [38] are employed in the $\mathscr{H}$-BE formulation.

Each of the FE–$\mathscr{H}$-BE coupling strategies outlined in the section 3 is employed to calculate the response in a frequency range between $0\,\mathrm{Hz}$ and $100\,\mathrm{Hz}$, with a frequency step of $1\,\mathrm{Hz}$. A maximum of 200 global iterations is prescribed for the iterative algorithms. Figure 3 shows the real and imaginary part of the radial displacement at $r = r_\mathrm{o}$, for the three values of the wave velocity ratio α introduced above. All methods yield accurate results in very good agreement with the analytical solution [39] for all values of the ratio α, with exception of the sequential Neumann–Dirichlet algorithm, which is unable to retrieve the correct solution at every frequency for a wave velocity ratio $\alpha = 1/2$ within the prescribed number of iterations.

The integral representation theorem subsequently allows for the computation of the radiated wavefield in the soil from the displacements and tractions on the FE–$\mathscr{H}$-BE interface. Figure 4 shows the real and imaginary part of the radial displacement at $r = 10\,\mathrm{m}$. The solutions of the various coupling procedures are clearly in good correspondence with each other and agree with the analytical solution, except for the aforementioned Neumann–Dirichlet algorithm.

Figures 3 and 4 validate the numerical implementation of the FE–$\mathscr{H}$-BE coupling strategies presented in this paper. The computational performance of each method strongly differs from one another, however. Figure 5 shows the CPU time required in each algorithm in function of the frequency, for the three wave velocity ratios considered. It is observed that the computation time in the direct coupling approach significantly exceeds the computational effort of the alternative procedures due to the drawbacks summarized in subsection 3.1, rendering the conventional method the least efficient. The computation time remains quasi independent of

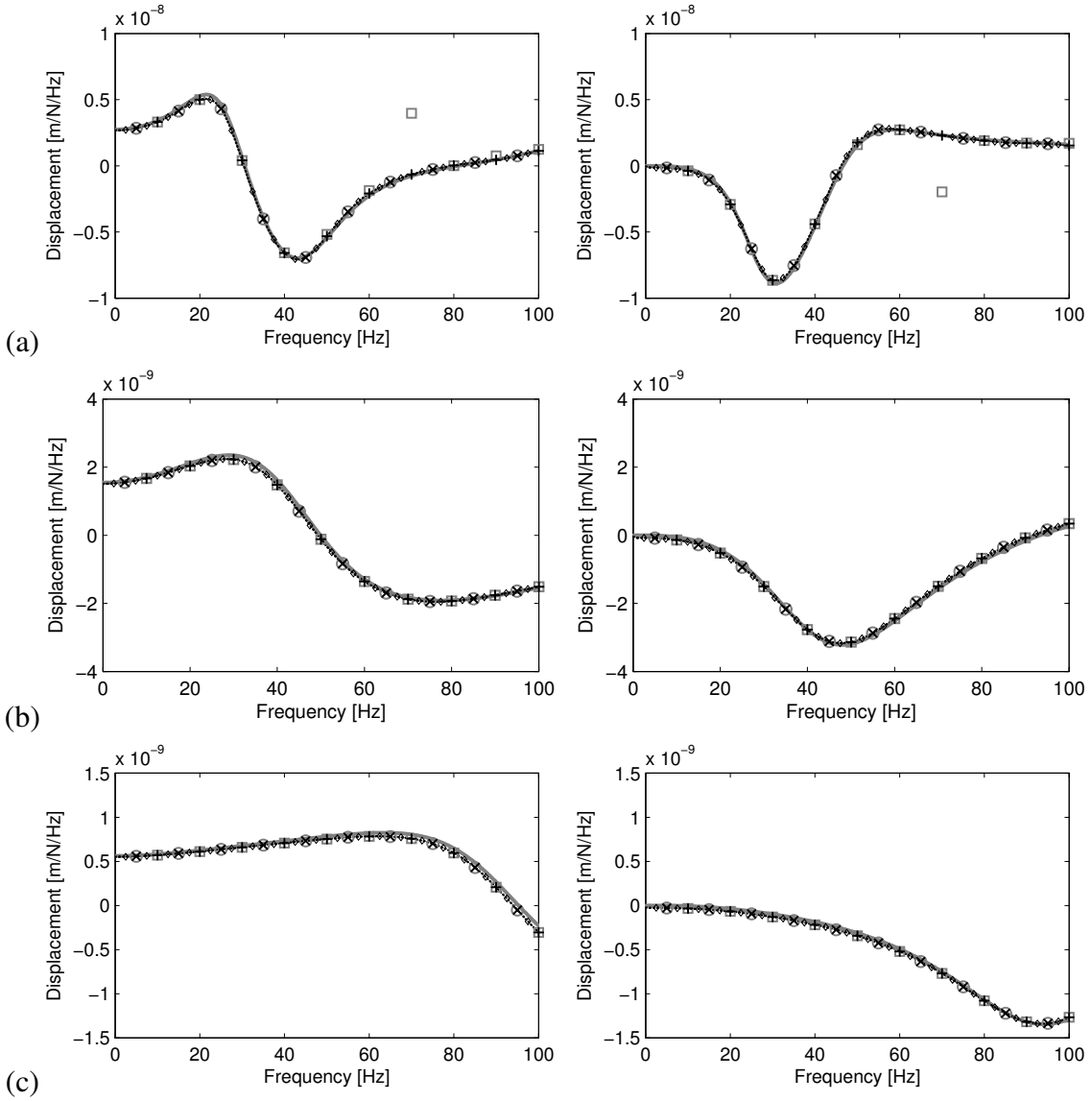

Figure 3: Real (left) and imaginary (right) part of the radial displacement at $r = r_{\mathrm{o}}$ due to a unit harmonic pressure applied to a spherical cavity surrounded by a spherical layer and a homogeneous full space, for (a) $\alpha = 1/2$, (b) $\alpha = 1$ and (c) $\alpha = 2$. The solutions of the classical direct coupling approach (dashed black line), the iterative Neumann–Dirichlet (grey squares), Dirichlet–Neumann (black plus signs), Neumann–Neumann (grey circles) and Dirichlet–Dirichlet (black crosses) algorithms, and the monolithic coupling procedure (black rhombuses) are compared to the analytical solution (solid grey line) [39].

the wave velocity ratio, but exhibits an increase with frequency. This is related to the fact that the time required to assemble and solve the set of $\mathscr{H}$-BE equations increases at higher frequencies [14], and such a trend is also observed for the other coupling methodologies. The computational efficiency of the iterative coupling schemes, however, is much stronger affected by the wave velocity ratio α. This is in particular the case for the sequential variants: the CPU time in the Neumann–Dirichlet algorithm strongly decreases for increasing values of α, while the reverse is observed for the Dirichlet–Neumann approach. This confirms the idea that Neumann boundary conditions should be applied to the most stiff subdomain in order to achieve the fastest convergence. The efficiency of the parallel iterative algorithms depends less

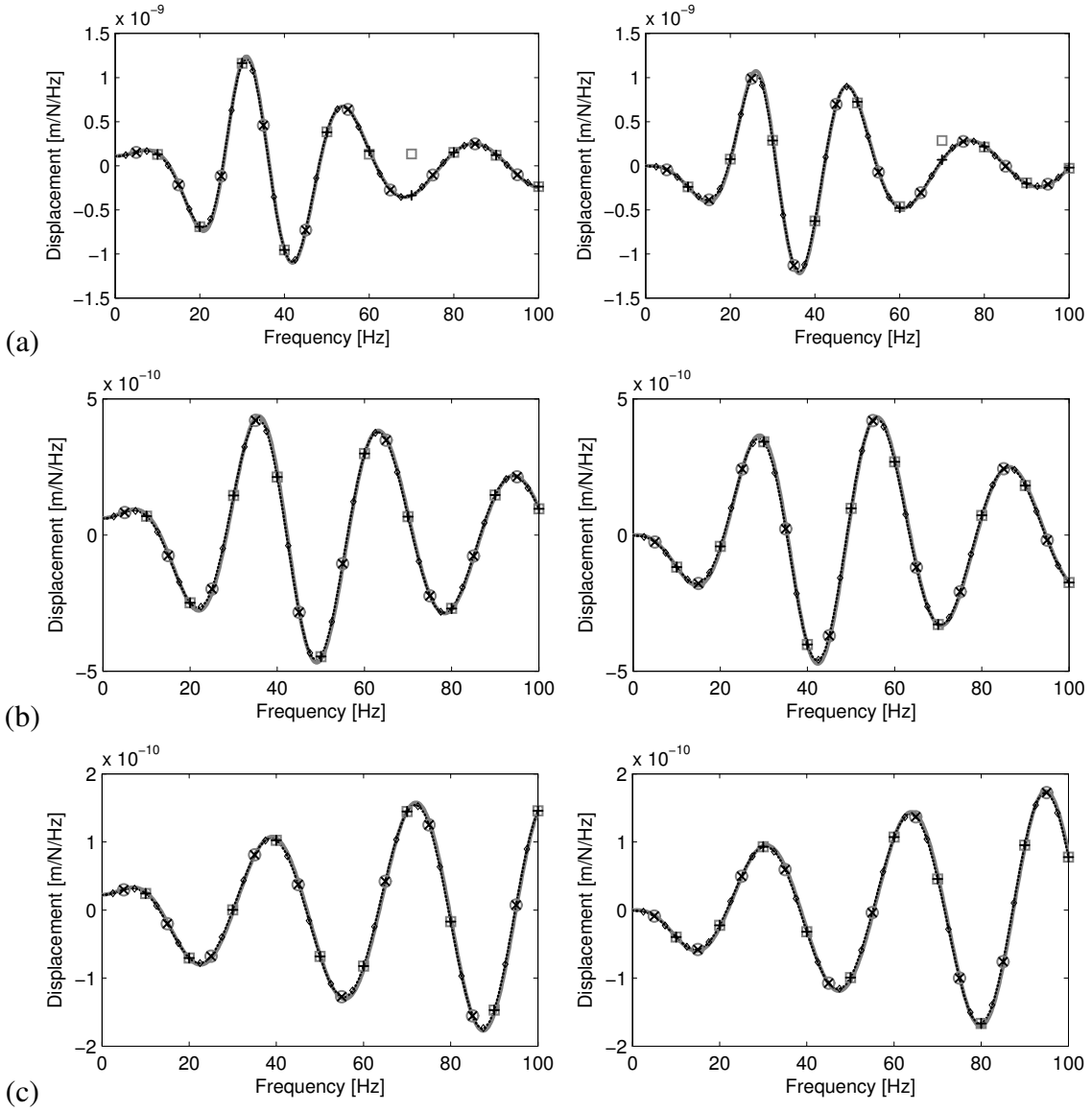

Figure 4: Real (left) and imaginary (right) part of the radial displacement at $r = 10\,\mathrm{m}$ due to a unit harmonic pressure applied to a spherical cavity surrounded by a spherical layer and a homogeneous full space, for (a) $\alpha = 1/2$, (b) $\alpha = 1$ and (c) $\alpha = 2$. The solutions of the classical direct coupling approach (dashed black line), the iterative Neumann–Dirichlet (grey squares), Dirichlet–Neumann (black plus signs), Neumann–Neumann (grey circles) and Dirichlet–Dirichlet (black crosses) algorithms, and the monolithic coupling procedure (black rhombuses) are compared to the analytical solution (solid grey line) [39].

strongly on α due to the relaxation procedure introduced in subsection 3.2.3, as the contribution of each subdomain to the relaxed interaction forces or displacements is balanced in every step of the iterative procedure. Finally, figure 5 illustrates that the monolithic coupling scheme is also relatively insensitive to the value of α, but the overall computational performance of this methodology remains relatively poor compared to the iterative algorithms. The implementation of a more rigorous preconditioner than the one applied in this paper might result in an improved convergence behaviour. Algebraic multigrid preconditioning strategies adapted for hierarchical matrices [40] or approaches based on the sparse approximate inverse (SPAI) of the BE matrices [10] are worthwhile to be considered in future research.

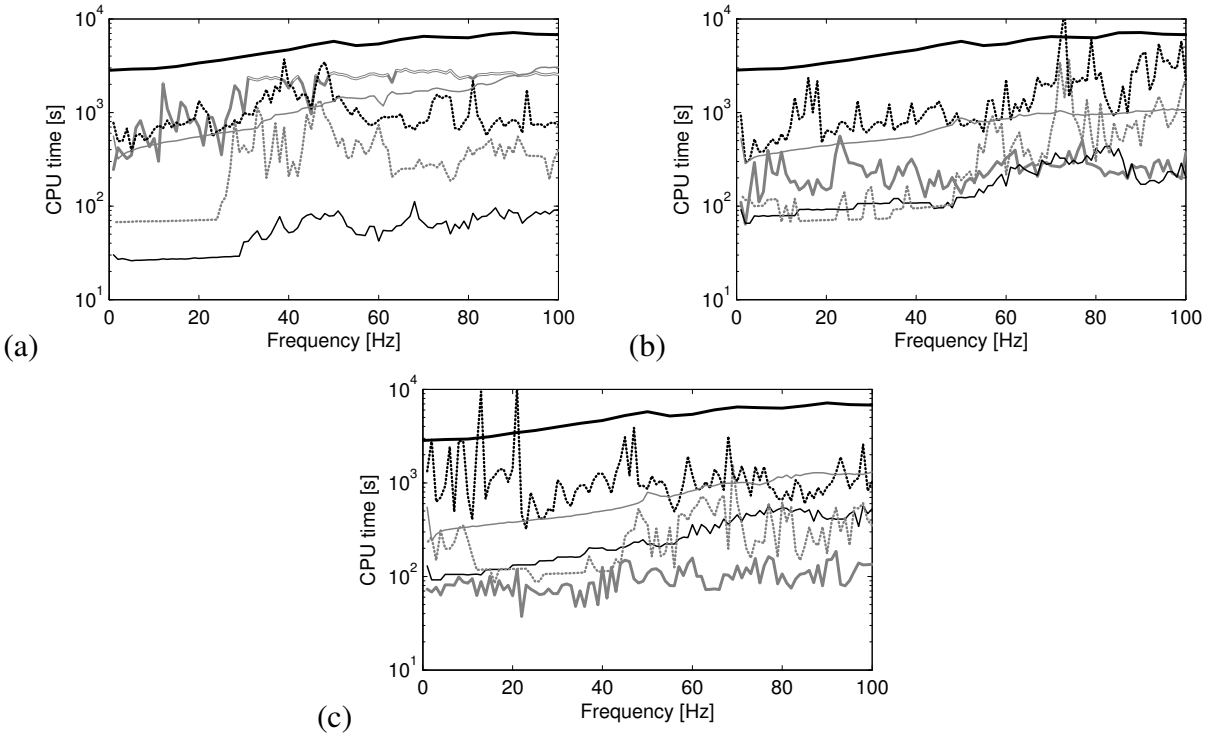

Figure 5: CPU time required in the classical direct coupling approach (thick black line), the iterative Neumann–Dirichlet (thick grey line), Dirichlet–Neumann (thin black line), Neumann–Neumann (dotted grey line) and Dirichlet–Dirichlet (dotted black line) algorithms, and the monolithic coupling procedure (thin grey line), for (a) $\alpha = 1/2$, (b) $\alpha = 1$ and (c) $\alpha = 2$. The lines are only drawn if the correct numerical solution is obtained.

Some important conclusions can be drawn from the results presented in figure 5. It is clear that the classical direct approach is not well suited to provide an efficient coupling of FE and $\mathscr{H}$-BE models; application of the alternative procedures is more appropriate. In particular, if there exists a strong stiffness contrast between the subdomains, a sequential iterative algorithm is preferred. It is recommended to impose Neumann boundary conditions on the most stiff subdomain; the reverse choice can significantly deteriorate the convergence behaviour. If such a contrast is not apparent, however, the parallel iterative algorithms as well as the monolithic approach provide a reliable and robust coupling of FE and $\mathscr{H}$-BE models.

The efficiency of the sequential iterative procedures is now investigated in more detail. In each global iterative step k, an iterative FGMRES solver is used to solve equation (4) for tractions $\hat{\underline{\mathbf{t}}}^{(k)}(\omega)$ or interface displacements $\hat{\underline{\mathbf{u}}}_2^{(k+\lambda)}(\omega)$ in the Neumann–Dirichlet or Dirichlet–Neumann algorithm, respectively. Figures 6 and 7 show the number of FGMRES–iterations in these algorithms in function of the frequency and the iteration step k. The number of FGMRES–iterations generally decreases in subsequent iteration steps, as the relaxed solution obtained in iteration $k-1$ is used as an initial guess in the FGMRES solver in iteration k. The number of global iterations strongly decreases for increasing values of α in figure 6, while the reverse is observed in figure 7.

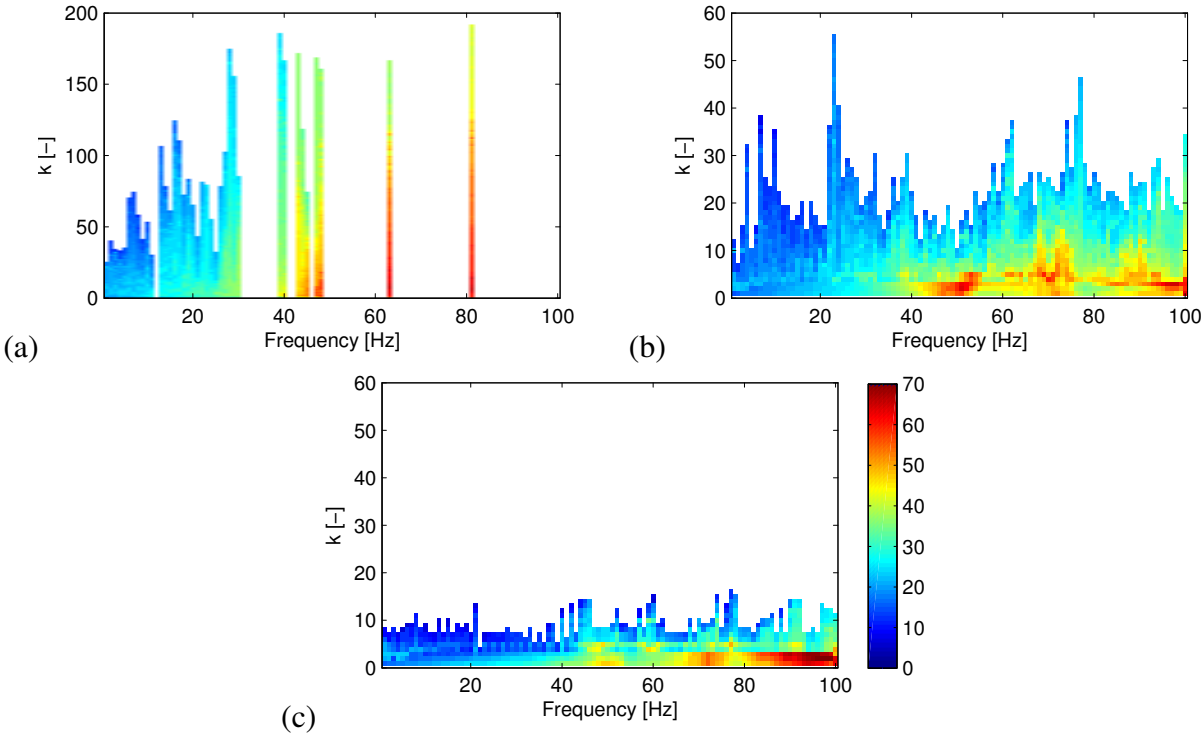

Figure 6: Number of FGMRES–iterations to solve the $\mathscr{H}$-BE equation (4) for tractions in the iterative Neumann–Dirichlet algorithm in function of the frequency and the iteration step k, for (a) $\alpha = 1/2$, (b) $\alpha = 1$ and (c) $\alpha = 2$. The bars are only drawn if the correct numerical solution is obtained.

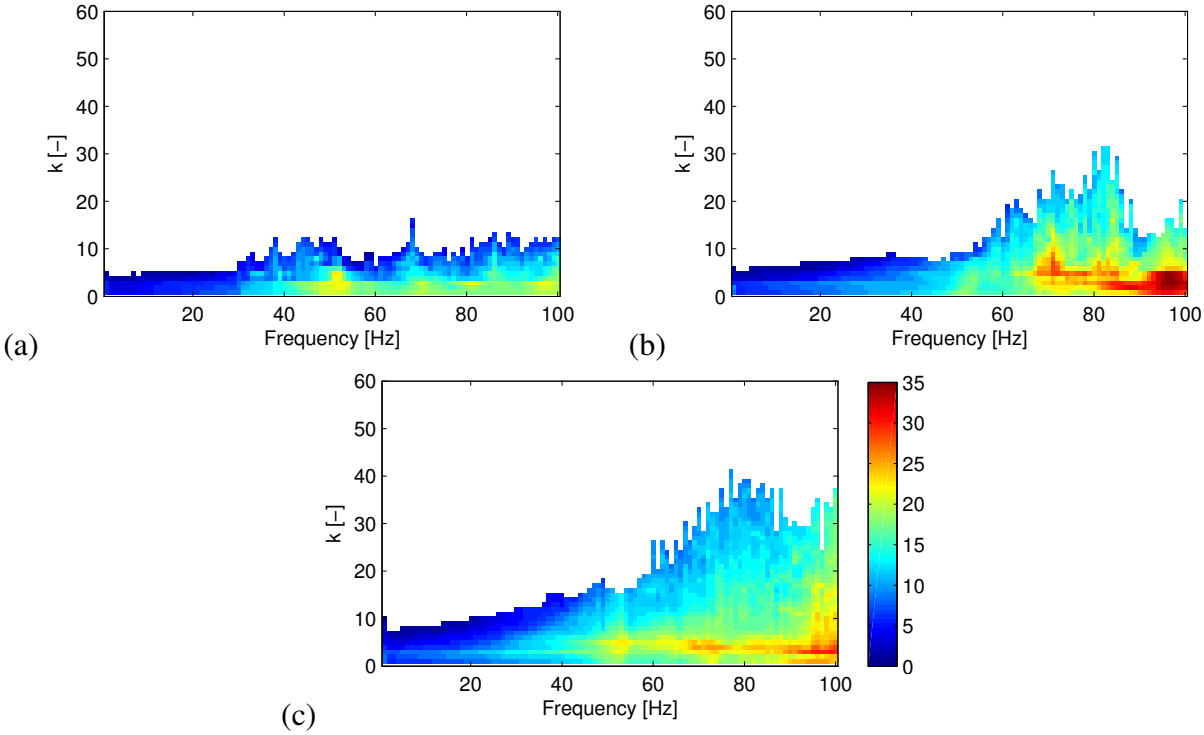

Figure 7: Number of FGMRES–iterations to solve the $\mathscr{H}$-BE equation (4) for interface displacements in the iterative Dirichlet–Neumann algorithm in function of the frequency and the iteration step k, for (a) $\alpha = 1/2$, (b) $\alpha = 1$ and (c) $\alpha = 2$.

Numerical simulations have furthermore demonstrated that application of Aitken's Δ^2–method for the interface relaxation is crucial in order to ensure convergence in the sequential iterative algorithms. No convergence could be obtained with these algorithms in any of the examples under concern in case a fixed value was attributed to the relaxation parameter $\lambda^{(k)}$ (where several constant values between 0 and 1 have been considered), in the entire frequency range of interest. Figure 8 shows the variation of $\lambda^{(k)}$ in the sequential Neumann–Dirichlet algorithm at a frequency of $100\,\mathrm{Hz}$ for $\alpha = 1$, clearly illustrating the dependency of the relaxation parameter on the iteration step.

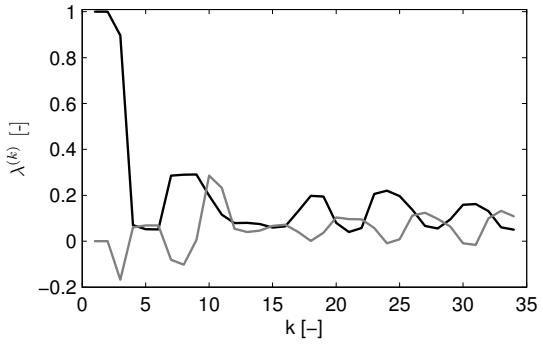

Figure 8: Real (black line) and imaginary (grey line) part of the Aitken relaxation parameter $\lambda^{(k)}$ at $100\,\mathrm{Hz}$ in the sequential Neumann–Dirichlet iterative algorithm, for $\alpha = 1$.

Finally, the effectiveness of the relaxation procedure for the parallel iterative algorithms introduced in subsection 3.2.3 is demonstrated. Figure 9 compares the CPU time in the iterative Neumann–Neumann algorithm using equation (15) for the determination of relaxed interaction forces $\hat{\underline{\mathbf{q}}}^{(k+1)}(\omega)$ to the cases where either $\hat{\underline{\mathbf{q}}}^{(k+1)}_{\mathrm{FE}}(\omega)$ or $\hat{\underline{\mathbf{q}}}^{(k+1)}_{\mathrm{BE}}(\omega)$ is employed, respectively. As indicated in subsection 3.2.3, the fastest convergence is achieved if the displacement discrepancy $\Delta\hat{\underline{\mathbf{u}}}^{(k)}_2(\omega)$ is imposed on the most flexible subdomain, i.e. on the FE subdomain for $\alpha = 1/2$ and on the BE subdomain for $\alpha = 2$. The reverse choice strongly affects the convergence behaviour, however, and the algorithm does even not convergence at some frequencies if $\hat{\underline{\mathbf{q}}}^{(k+1)}_{\mathrm{BE}}(\omega)$ is employed for $\alpha = 1/2$. The relaxation procedure corresponding to equation (15) proves to be a reliable alternative, as the associated CPU times only moderately depend on α and are often bounded by the computation times of the two other approaches.

4.2 Flexible surface foundation on a horizontally layered halfspace

A flexible square surface foundation resting on a horizontally layered halfspace is considered in this subsection. The foundation has dimensions $5\,\mathrm{m} \times 5\,\mathrm{m} \times 0.25\,\mathrm{m}$ and consists of concrete with a Young's modulus $E = 33\,\mathrm{GPa}$, a Poisson's ratio $\nu = 0.20$, and a density $\rho = 2500\,\mathrm{kg/m^3}$. Rayleigh damping is assumed, allowing to write the frequency independent proportional damping matrix as $\mathbf{C} = a_0\mathbf{M} + a_1\mathbf{K}$. The Rayleigh damping coefficients a_0 and a_1 are determined by attributing a modal damping ratio $\xi = 0.03$ to the first two non rigid body modes. As indicated in subsection 3.2.1, structural damping is included to avoid singularity of the FE equations if a sequential Neumann–Dirichlet algorithm is employed. A unit harmonic vertical point excitation is applied to the center of the foundation, within a frequency range between $0\,\mathrm{Hz}$ and $100\,\mathrm{Hz}$.

The soil consists of two layers on a halfspace, each with a thickness of $2\,\mathrm{m}$. The shear wave

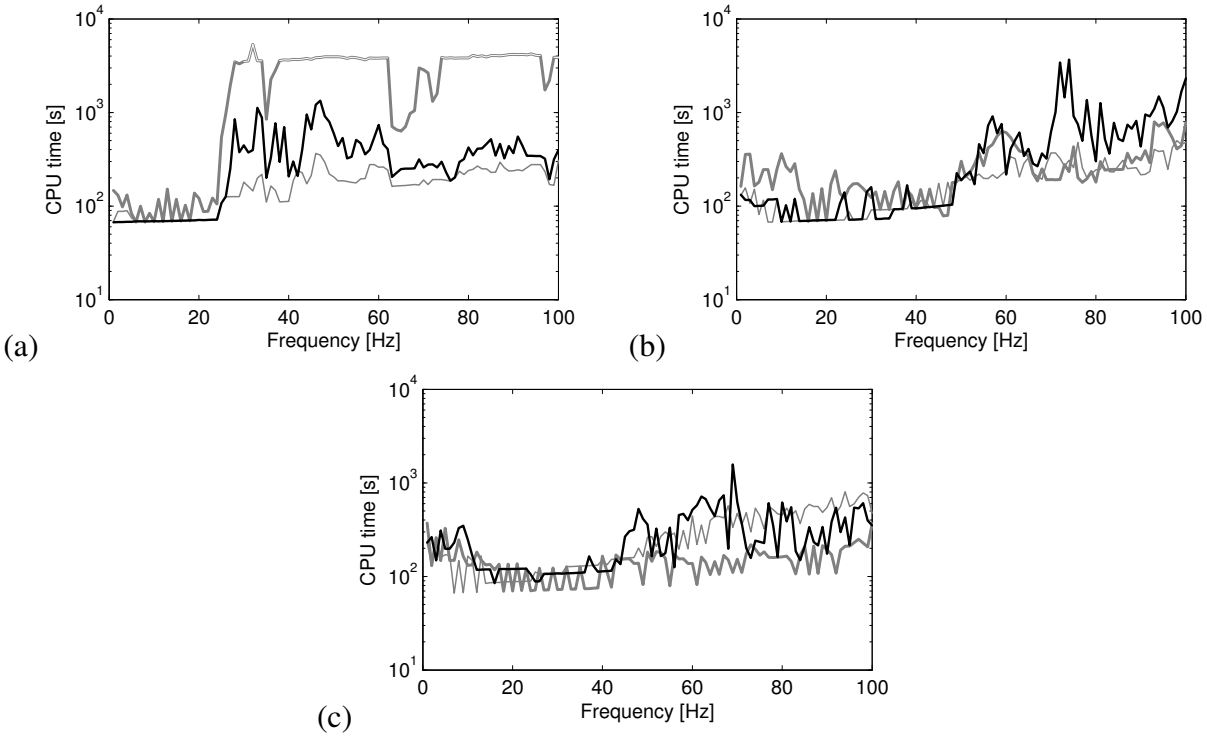

Figure 9: CPU time required in the parallel Neumann–Neumann algorithm in case the displacement discrepancy is imposed on the BE subdomain (thick grey line), on the FE subdomain (thin grey line), and in case the relaxation procedure corresponding to equation (15) is employed (black line), for (a) $\alpha = 1/2$, (b) $\alpha = 1$ and (c) $\alpha = 2$. The lines are only drawn if the correct numerical solution is obtained.

velocity C_s is equal to $150\,\mathrm{m/s}$ in the top layer, $250\,\mathrm{m/s}$ in the second layer, and $300\,\mathrm{m/s}$ in the underlying halfspace. The Poisson's ratio ν is $1/3$ everywhere, resulting in dilatational wave velocities C_p of $300\,\mathrm{m/s}$, $500\,\mathrm{m/s}$, and $600\,\mathrm{m/s}$, respectively. Material damping ratios $\beta_\mathrm{s} = \beta_\mathrm{p} = 0.025$ in both deviatoric and volumetric deformation are attributed to the layers and the halfspace, while a uniform density $\rho = 1800\,\mathrm{kg/m^3}$ is considered throughout the medium.

The foundation is discretized by means of 30×30 equally sized shell elements based on Kirchhoff plate theory, which are coupled to a conforming BE mesh using a nodal collocation scheme for the soil. Up to nine elements per shear wavelength $\lambda_\mathrm{s} = C_\mathrm{s}/f$ are provided at the maximum frequency of $100\,\mathrm{Hz}$ (determined by the shear wave velocity of the top layer). Green's functions for a layered halfspace are incorporated in the $\mathscr{H}$-BE formulation [14, 15, 41], avoiding the necessity to discretize the free surface and the layer interfaces. It is expected that the foundation will behave much stiffer than the soil in the frequency range of interest. In accordance with the findings of subsection 4.1, an iterative Neumann–Dirichlet coupling scheme is therefore employed. The monolithic coupling approach is considered as well.

Figure 10 shows the real and imaginary part of the vertical displacement $\hat{u}_z(\mathbf{x}, \omega)$ at the center of the foundation, calculated with both coupling procedures; a perfect agreement between the results is observed. The iterative Neumann–Dirichlet is unable, however, to determine the static solution, and the frequency sweep is therefore performed from high to low frequencies. The vertical displacement of the foundation and the surrounding soil is shown in figures 11a and 11b at $25\,\mathrm{Hz}$ and $100\,\mathrm{Hz}$, respectively. While the wave fronts at the surface of the soil remain almost perfectly cylindrical at $25\,\mathrm{Hz}$, this is no longer the case at $100\,\mathrm{Hz}$ due to the dynamic interaction between the foundation and the soil.

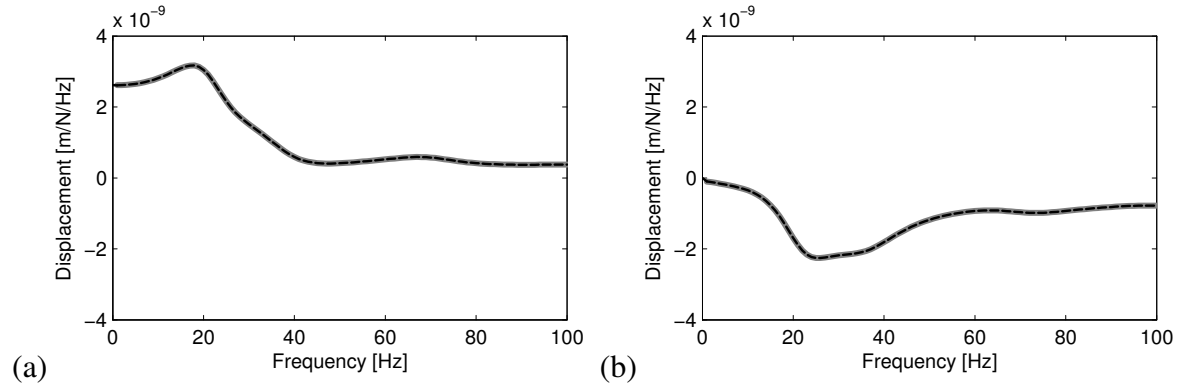

Figure 10: (a) Real and (b) imaginary part of the vertical displacement $\hat{u}_z(\mathbf{x}, \omega)$ at the center of a flexible surface foundation on a layered halfspace excited by a unit harmonic vertical point load. The solution of the iterative Neumann–Dirichlet algorithm (grey solid line) is compared to the solution of the monolithic coupling procedure (black dashed line).

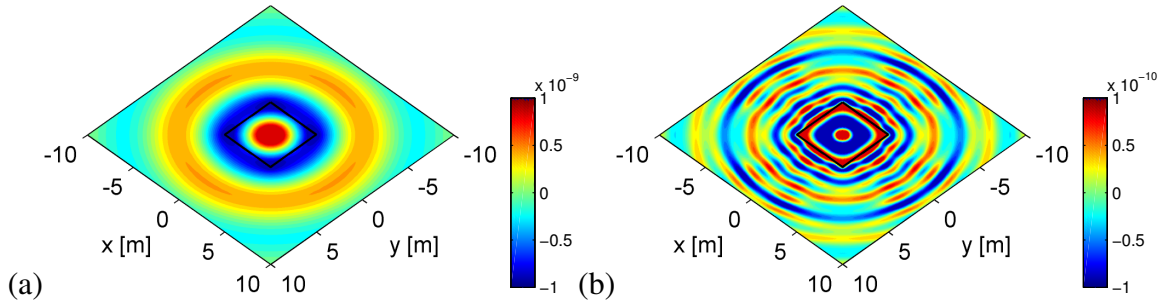

Figure 11: Real part of the vertical displacement $\hat{u}_z(\mathbf{x}, \omega)$ of the foundation and the soil for a flexible surface foundation on a layered halfspace excited at its center by a unit harmonic vertical point load at (a) $25\,\mathrm{Hz}$ and (b) $100\,\mathrm{Hz}$.

Figure 12a shows the number of FGMRES–iterations in function of the frequency and the iteration step k for the sequential Neumann–Dirichlet algorithm. Imposing the relaxed interaction forces obtained in step $k-1$ as initial guess in the FGMRES–solver of step k is clearly beneficial, as the number of FGMRES–iterations in subsequent steps is strongly reduced. This number remains almost constant, however, if no initial guess is used (figure 12b). Furthermore, employing the converged solution at a particular frequency as initial guess in the first iteration at the next frequency is also advantageous, resulting in a lower number of iteration steps in the iterative algorithm. Peaks at $40\,\mathrm{Hz}$ and $62\,\mathrm{Hz}$ correspond to natural frequencies of the foundation.

5 CONCLUSIONS

In this paper, the coupling of FE and $\mathscr{H}$-BE methods has been discussed, illustrating that a subdomain approach is well suited to efficiently solve dynamic SSI problems in the frequency domain. The application of $\mathscr{H}$–matrices enables the fast evaluation of large BE models, and the incorporation of Green's functions for a layered halfspace avoids the need to discretize the free surface and the layer interfaces in the modelling of visco–elastodynamic wave propagation in a stratified medium.

Direct, iterative and monolithic coupling strategies have been considered throughout this

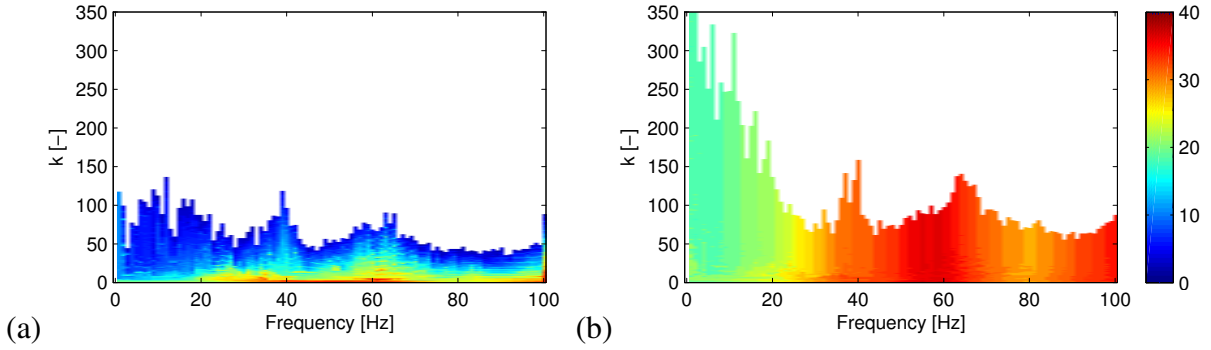

Figure 12: Number of FGMRES–iterations to solve the $\mathscr{H}$-BE equation (4) for tractions in the iterative Neumann–Dirichlet algorithm in function of the frequency and the iteration step k, for a flexible surface foundation on a layered halfspace. The numbers are shown (a) in case the relaxed tractions in iteration $k-1$ are used as an initial guess in iteration k, while the converged solution at a particular frequency is used as an initial guess for the first iteration at the subsequent frequency, or (b) in case no initial guess is provided in the FGMRES solver.

paper, and the numerical validation of each algorithm is presented. An assessment of the computational performance reveals that the direct coupling approach is the least efficient, as the assembly of a dynamic soil stiffness matrix requires the solution of a large amount of $\mathscr{H}$–BE equations. Iterative coupling procedures are more efficient, provided that suitable boundary conditions are applied to each subdomain. It is demonstrated that sequential iterative algorithms should be preferred if there exists a strong stiffness contrast between the FE and $\mathscr{H}$-BE subdomain, with Neumann boundary conditions to be imposed on the most stiff subdomain. The application of Aitken's Δ^2–method for the determination of a proper interface relaxation parameter ensures and speeds up the convergence of these sequential algorithms. Parallel iterative algorithms provide a valuable alternative for cases where an a priori estimation of the flexibility of each subdomain is not obvious, and an appropriate relaxation procedure has been proposed for these algorithms. An efficient combination of FE and $\mathscr{H}$–BE models can also be achieved by means of a monolithic coupling scheme, although the convergence in the examples considered turns out to be relatively slow. This might be improved by the incorporation of an enhanced preconditioner; this is the subject of further research.

ACKNOWLEDGEMENTS

The first author is a doctoral fellow and the second author is a postdoctoral fellow of the Research Foundation Flanders (FWO). The financial support is gratefully acknowledged.

REFERENCES

[1] J.-F. Semblat, A.M. Duval, and P. Dangla. Seismic site effects in a deep alluvial basin: numerical analysis by the boundary element method. *Computers and Geotechnics*, 29(7):573–585, 2002.

[2] G. Lombaert, G. Degrande, and D. Clouteau. Numerical modelling of free field traffic induced vibrations. *Soil Dynamics and Earthquake Engineering*, 19(7):473–488, 2000.

[3] D.E. Beskos, T. Krauthammer, and I. Vardoulakis, editors. *Dynamic soil-structure interaction*. A.A. Balkema, 1984.

[4] O. Von Estorff and C. Hagen. Iterative coupling of FEM and BEM in 3D transient elastodynamics. *Engineering Analysis with Boundary Elements*, 29:775–787, 2005.

[5] D. Clouteau, M.L. Elhabre, and D. Aubry. Periodic BEM and FEM-BEM coupling: application to seismic behaviour of very long structures. *Computational Mechanics*, 25:567–577, 2000.

[6] O.C. Zienkiewicz, D.W. Kelly, and P. Bettes. The coupling of the finite element method and boundary solution procedures. *International Journal for Numerical Methods in Engineering*, 11:355–375, 1977.

[7] G.C. Hsiao. The coupling of boundary element and finite element methods. *Zeitschrift für Angewandte Mathematik und Mechanik*, 70:493–503, 1990.

[8] M. Costabel and E.P. Stephan. Coupling of finite and boundary element methods for an elastoplastic interface problem. *SIAM Journal on Numerical Analysis*, 27(5):1212–1226, 1990.

[9] W.M. Elleithy, H. J. Al-Gahtani, and M. El-Gebeily. Iterative coupling of BE and FE methods in elastostatics. *Engineering Analysis with Boundary Elements*, 25:685–695, 2001.

[10] M. Margonari and M. Bonnet. Fast multipole method applied to elastostatic BEM-FEM coupling. *Computers and Structures*, 83(10–11):700–717, 2004.

[11] T. Rüberg and M. Schanz. Coupling finite and boundary element methods for static and dynamic elastic problems with non-conforming interfaces. *Computer Methods in Applied Mechanics and Engineering*, 198(3–4):449–458, 2008.

[12] S. Chaillat, M. Bonnet, and J.-F. Semblat. A multi-level fast multipole BEM for 3-D elastodynamics in the frequency domain. *Computer Methods in Applied Mechanics and Engineering*, 197(49–50):4233–4249, 2008.

[13] W. Hackbusch. A sparse matrix arithmetic based on $\mathscr{H}$-matrices. Part I: Introduction to $\mathscr{H}$-matrices. *Computing*, 62(2):89–108, 1999.

[14] P. Coulier, S. François, G. Lombaert, G. Degrande, A hierarchical boundary element method for elastodynamics based on Green's functions for a horizontally layered halfspace, Engineering Analysis with Boundary Elements, Submitted for publication.

[15] E. Kausel and J.M. Roësset. Stiffness matrices for layered soils. *Bulletin of the Seismological Society of America*, 71(6):1743–1761, 1981.

[16] L. Grasedyck and W. Hackbusch. Construction and arithmetics of $\mathscr{H}$-matrices. *Computing*, 70:295–334, 2003.

[17] S. Rjasanow and O. Steinbach. *The Fast Solution of Boundary Integral Equations (Mathematical and Analytical Techniques with Applications to Engineering)*. Springer-Verlag New York, 2007.

[18] M. Bebendorf and S. Rjasanow. Adaptive low–rank approximation of collocation matrices. *Computing*, 70:1–24, 2003.

[19] M. Bebendorf. *Hierarchical Matrices: A Means to Efficiently Solve Elliptic Boundary Value Problems*. Springer Publishing Company, 1st edition, 2008.

[20] Y. Saad and M.H. Schultz. GMRES: a generalized minimal residual algorithm for solving nonsymmetric linear systems. *SIAM Journal on Scientific and Statistical Computing*, 7(3):856–869, 1986.

[21] M. Bebendorf. Hierarchical LU decomposition based preconditioners for BEM. *Computing*, 74:225–247, 2005.

[22] Y. Saad. A flexible inner-outer preconditioned GMRES algorithm. *SIAM Journal on Scientific and Statistical Computing*, 14(2):461–469, 1993.

[23] S. Chaillat, J.-F. Semblat, and M. Bonnet. A preconditioned 3-D multi-region fast multipole solver for seismic wave propagation in complex geometries. *Communications in Computational Physics*, 11(2):594–609, 2012.

[24] O. Von Estorff and E. Kausel. Coupling of boundary and finite elements for soil-structure interaction. *Earthquake Engineering and Structural Dynamics*, 18:1065–1075, 1989.

[25] O. Von Estorff and M. Firuziaan. Coupled BEM/FEM approach for nonlinear soil/structure interaction. *Engineering Analysis with Boundary Elements*, 24:605–621, 2000.

[26] S. François, H.R. Masoumi, and G. Degrande. An iterative coupled boundary-finite element method for the dynamic response of structures. In P. Sas and M. De Munck, editors, *Proceedings of ISMA2006 International Conference on Noise and Vibration Engineering*, pages 1701–1716, Leuven, Belgium, September 2006.

[27] D. Soares Jr. and L. Godinho. An optimized BEM–FEM iterative coupling algorithm for acoustic–elastodynamic interaction analyses in the frequency domain. *Computers and Structures*, 106–107:68–80, 2012.

[28] D. Soares Jr., L. Godinho, A. Pereira, and C. Dors. Frequency domain analysis of acoustic wave propagation in heterogeneous media considering iterative coupling procedures between the method of fundamental solutions and Kansa's method. *International Journal for Numerical Methods in Engineering*, 89(7):914–938, 2012.

[29] E. Grasso. *Modelling visco-elastic seismic wave propagation: a fast-multipole boundary element method and its coupling with finite elements*. PhD thesis, Université Paris-Est, 2012.

[30] W.M. Elleithy and M. Tanaka. Interface relaxation algorithms for BEM-BEM coupling and FEM-BEM coupling. *Computer Methods in Applied Mechanics and Engineering*, 192:2977–2992, 2003.

[31] C. Hagen. *Wechselwirkungen zwischen Bauwerk, Boden und Fluid unter transienter Belastung*. PhD thesis, Technischen Universität Hamburg-Harburg, 2005.

[32] A.C. Aitken. Studies in practical mathematics II: The evaluation of the latent roots and latent vectors of a matrix. *Proceedings of the Royal Society of Edinburgh*, 57:269–304, 1937.

[33] D.P. Mok, W.A. Wall, and E. Ramm. Accelerated iterative substructuring schemes for instationary fluid-structure interaction. In K.J. Bathe, editor, *Computational Fluid and Solid Mechanics*, pages 1325–1328. Elsevier, 2001.

[34] U. Küttler and W.A. Wall. Fixed-point fluid-structure interaction solvers with dynamic relaxation. *Computational Mechanics*, 43(1):61–72, 2008.

[35] B.M. Irons and R.C. Tuck. A version of the Aitken accelerator for computer iteration. *International Journal for Numerical Methods in Engineering*, 1(3):275–277, 1969.

[36] B. Hübner, E. Walhorn, and D. Dinkler. A monolithic approach to fluid-structure interaction using space-time finite elements. *Computer Methods in Applied Mechanics and Engineering*, 193(23–26):2087–2104, 2004.

[37] C. Michler, S.J. Hulshoff, E.H. van Brummelen, and R. de Borst. A monolithic approach to fluid-structure interaction. *Computers and Fluids*, 33:839–848, 2004.

[38] E. Kausel. *Fundamental solutions in elastodynamics: a compendium*. Cambridge University Press, New York, 2006.

[39] S. Chaillat, M. Bonnet, and J.-F. Semblat. A new fast multi-domain BEM to model seismic wave propagation and amplification in 3D geological structures. *Geophysical Journal International*, 177:509–531, 2009.

[40] U. Langer and D. Pusch. Data-sparse algebraic multigrid methods for large scale boundary element equations. *Applied Numerical Mathematics*, 54(3–4):406–424, 2005.

[41] M. Schevenels, S. François, and G. Degrande. EDT: An ElastoDynamics Toolbox for MATLAB. *Computers & Geosciences*, 35(8):1752–1754, 2009.